

RF Energy Harvesting for Battery-Less and Maintenance-Free Condition Monitoring of Railway Tracks

Pengyu Li, Zhihe Long, and Zhengbao Yang, *Member, IEEE*

Abstract—Current railway track condition monitoring relies on inefficient human inspectors and expensive inspection vehicles, where high-frequency inspection is unreachable since these methods occupy the tracks. This paper proposes a battery-less railway monitoring system based on RF energy harvesting to detect early defects on rail tracks. The key part of the system is a battery-less wireless sensor tag (BLWST) installed on railway tracks. The BLWST can harvest RF energy from a reader installed on the train, and precisely measure and wirelessly transmit vibration condition of tracks back to the reader. The proposed system eliminates the demands for cables and battery replacement, thus achieving low installation and maintenance cost. The high-frequency monitoring also provides a more reliable inspection than existing methods. The BLWST is based on the 3-stage Dickson voltage multiplier (DVM) and can be activated by a dedicated RF power source at a maximum distance of 2.3 meters. Experiments show that a maximum energy conversion efficiency of 25% and 500 working cycles per second are achieved. For demonstration, we construct a miniaturized railway system with the battery-less prototype and exhibit a reliable wireless power transfer and data communication.

Index Terms—Dickson voltage multiplier, Internet of Things, RF energy harvesting, railway tracks inspection, structural health monitoring.

I. INTRODUCTION

RAILWAY is an economical and low-CO₂-emission way of land transportation [1]. The demand for traveling and easing traffic congestion leads to the rapid growth of the railway length in China in the last decade. A railway length of 22,000 km and a passenger volume of 1.44 billion were recorded in 2016, and such a high ridership heavily burdens the railway system [2]. The stress and impact on the railway tracks introduced by the interaction between the train wheels and the tracks deteriorate the track quality over time [3]. Therefore, it is vital to frequently inspect and report the condition of the railway tracks for discovering the potential risks in time [4]. The current rail tracks inspection mainly relies on the low-efficiency, costly, and dangerous manual approach. There are also effective mobile tools and customized vehicles equipped with inspection systems that can speed up the

Pengyu Li, Zhihe Long, and Zhengbao Yang are with Department of Mechanical Engineering, City University of Hong Kong, 83 Tat Chee Avenue, Kowloon Tong, Kowloon, Hong Kong SAR, China. Corresponding author: Zhengbao Yang (zb.yang@cityu.edu.hk).

checking work. For example, the ultrasonic and induction techniques are two common solutions for effectual railway inspection. Both of the two means operate well within a lift-off distance with the sensing probes arranged near the tracks [5], [6], [7], [8]. However, the shortages of these two approaches are that tracks will be occupied during device operation and still costly [9]. For these reasons, the inspection can only be executed at a low frequency. Consequently, the defects may not be discovered in time, resulting in accidents. To detect the defects timely, structural health monitoring inspired by Internet of Things (IoT) is an efficient inspection strategy without affecting the normal operation of the railway system and to reduce expenses [10]. The track defects can be identified promptly and automatically by installing massive low-cost wireless sensors on tracks [11]. However, the power supply for these sensors is a huge challenge since wired power is impractical for such a widely-distributed wireless sensor network [12], [13]. Also, replacing batteries is uneconomical and labour-consuming. Batteries suffer from current leakage and limited energy capacity issue. Moreover, the breaks of the batteries attributed to the extreme weather conditions may lead to chemical leakage that is harmful to the environment [14].

Energy harvesting can realize an extremely long-time energy supply for electronic devices especially wireless sensors by gathering and transferring ambient energies into electrical energy [15], [16], [17], [18], [19]. For example, Bischoff et al. [20] measured the strain of a railway bridge by using wireless sensor nodes and a base station powered by solar energy. However, this kind of energy heavily depends on weather and solar planes suffer from contamination of dust. There are also investigations on transferring the vibration of rail tracks into electrical power. For instance, Wischke et al. [12] attempted to harvest the energy from vibration caused by the train in a tunnel using a piezoelectric transducer. Yuan et al. [21] proposed a piezoelectric transducer to harvest the energy from the vibration of railway tracks as well. Gao et al. [13] described a wireless sensor node for railway monitoring powered by a rechargeable battery that is charged by a magnetic levitation energy harvester. Wang et al. [1] developed a mechanical based vibration energy harvester consisting of complex mechanical parts that deliver the energy to an electromagnetic generator. Zuo et al. [22] designed an electromagnetic energy harvester

for freight railcars. More researches on vibration energy harvesters refer to [23]. However, the efficiency of these harvesters can be greatly affected by the vibration condition that varies with different tracks and trains, and none of these designs demonstrates a fully battery-less operation.

Compared with the aforementioned solar-based and vibration-based energy harvesting, radio frequency (RF) energy harvesting is weather-independent and highly controllable [19]. RF energy can be generated from a dedicated RF power source and transferred to the harvester target only when needed [24]. A typical RF energy harvesting application is radio frequency identification (RFID), a popular technology applied in identifying objects [25]. The classic RFID system architecture is comprised of a reader, antennas, and a tag including the coded ID information [26], [27]. In the railway industry, RFID technology is employed to track the location and speed of the train [28]. However, conventional RFID technology is not capable of doing computation or sensing, and therefore not suitable for structural health monitoring.

The battery-less operation of wireless health monitoring sensors powered by RF energy can be realized by integrating sensors into the RFID tag [29]. For example, Qian et al. [30] developed a passive RFID tag with an embedded temperature sensor to observe the temperature of the axle of trains. Lee et al. [31] developed an active RFID temperature sensor for monitoring the transformer on the train. These designs primarily concentrate on tracking the on-train condition.

To our best knowledge, there is no report about the battery-less and wireless railway tracks monitoring. To fill this gap, we propose a low-cost and self-powered railway tracks inspection system using the RF energy harvesting technology. The system will shift the current labour-intensive and high-cost rail inspection that is usually scheduled once per several months [32], to an automatic, high-frequency, and maintenance-free condition monitoring method. Rail tracks will not just serve as passive structural supports anymore, but also play the role of smart active responders, which will significantly improve the reliability and safety of the railway system. The proposed system possesses the following superiorities:

- Allowing non-destructive and battery-less monitoring of the railway tracks condition, and therefore cutting down the operation cost.
- Supporting a high-frequency inspection since it does not occupy the railway, thus increasing the reliability and efficiency.
- Automatic sensing and transmitting data requiring no labour, and therefore promoting safety.

The contributions of this research are concluded as follows:

- We evaluate the performance of the rectifier constructed with HSMS-2862 diodes under different input powers and

distances. An end to end efficiency of 25 % is achieved, compared to the peak efficiency of 16 % in [33]. We also design an embedded wireless sensor consisting of CC430F5137 wireless transceiver and ADXL362 accelerometer with minimized energy consumption.

- We demonstrate the battery-less operation of the proposed BLWST and verify the accuracy of the data using a precise L215M vibration shaker. Besides, we investigate the achievable working cycles per unit time at different input powers and distances. Experiments show that the BLWST can work under a minimum input power of -5 dBm and a maximum distance of 2.3 meters.

The rest of the paper is organized as follows. Section II introduces the design of the proposed system. Section III presents the key components of the battery-less wireless sensor tag (BLWST), including the Dickson voltage multiplier (DVM), the embedded wireless sensor (EWS), and the power management unit. The performance evaluation experiments on RF energy harvesting and wireless sensing are described in Section IV, followed by the railway tracks monitoring test in Section V and conclusion in Section VI.

II. SYSTEM OVERVIEW

A. Architecture of the Proposed System

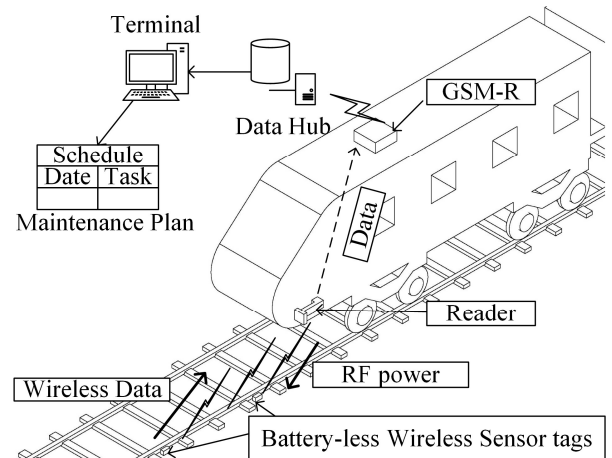


Fig. 1. The proposed railway monitoring system based on the RF energy harvesting. It consists of battery-less wireless sensor tags installed on the railway tracks and readers equipped on the train.

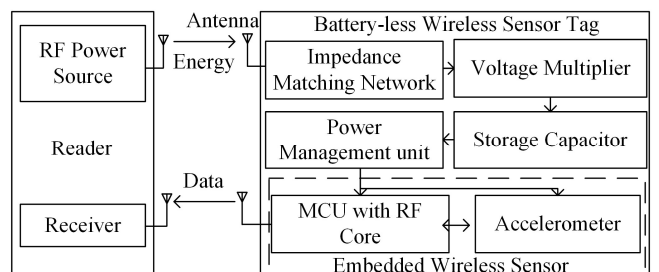


Fig. 2. Block diagram of the proposed battery-less railway monitoring system. It mainly consists of an RF power source, a receiver, and a battery-less wireless sensor tag.

Figure 1 shows the proposed wireless and self-powered sensor system for railway tracks inspection. The system is mainly constructed with BLWSTs installed on tracks and reader modules carried by the running train. The power needed for powering the tags is obtained from the readers through RF energy harvesting, and then the readers receive the track health information measured and wirelessly transmitted by BLWSTs. After receiving the data, the reader transfers the data to an on-train GSM communication system through a wired communication module such as the universal asynchronous receiver/transmitter (UART). The railway condition data will be sent to the control centers through the on-train GSM communication system such as GSM-R [34] to help to design condition-based maintenance and prevent accidents. Compared with the widely-used manual checks or customized measuring trains, the proposed solution can realize high-frequency and labour-free automatic monitoring, and thus attains better reliability and lower cost. Figure 2 depicts the detailed functional blocks of the proposed railway monitoring system, which consists of an RF power source, a receiver, and a BLWST. The reader module is a combination of the RF power source and receiver. Its function is to radiate RF energy and receive wireless information. The BLWST powered by the RF energy is responsible for sensing and transmitting the condition data of the railway tracks. The emitted RF energy from the RF power source will be captured and converted to AC power by the antenna of the BLWST. The generated AC power flows through the impedance matching circuit that ensures a high efficiency. Then, a voltage multiplier rectifies and multiplies the AC power to DC power, so that the harvested energy can be accumulated in the storage capacitor eventually. A power management unit integrated with a DC-DC converter extracts energy from the storage capacitor and powers the EWS comprised of an accelerometer and a microcontroller (MCU) with RF core.

B. Theoretical Estimation of the Available Wireless Power

The propagation of the RF power can be described by the Friis equation, as expressed in (1),

$$P_r(\text{dB}) = P_t + G_t + G_r + 20 \log(\lambda / 4\pi d) \quad (1)$$

where P_r refers to the power received by the receiver; P_t is the transmitted power; G_t is the gain of the antenna of RF power source whereas G_r represents the gain of the receiver antenna; λ is the wavelength of the target frequency, and d is the distance between RF power source and the receiver.

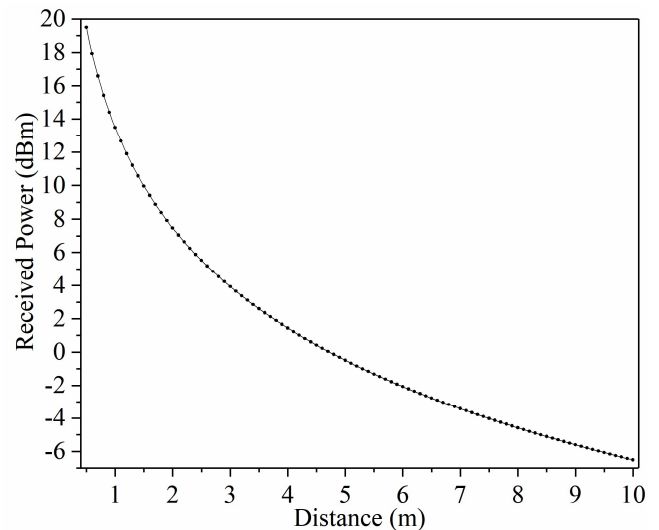


Fig. 3. Estimated received power as a function of the distance between the battery-less wireless sensor tag and the RF power source. The estimation is based on (1). The gains of the antennas are 6.1 dBi and 3 dBi, respectively. The wavelength (λ) is 0.33 m. The equivalent isotropic radiated power (EIRP) is 42 dBm.

The frequency of the used RF power is 915 MHz, a license-free and commonly-used frequency. A commercial omnidirectional antenna with a gain of 3 dBi and a directional antenna with a gain of 6.1 dBi were selected for harvesting the RF power and transmit the RF power, respectively. We customized an RF power source by combining a signal generator (ADF4350), an RF power amplifier (PF01411A) operating at 915 MHz with a maximum output power of 4 W (36 dBm) and a 6.1 dBi antenna for generating an equivalent isotropic radiated power (EIRP) of 42 dBm. And by replacing the amplifier with KDT0307B-006, a 36 dBm EIRP can be obtained as well.

Substituting the known parameters into (1), the estimated available RF power at the receiver can be calculated out, as shown in Fig. 3. We can observe that the theoretically available power heavily depends on the propagation path length, and the broadcast RF power exponentially declines as the distance increases. The available power is less than 0 dBm (1 mW) when the distance exceeds 5 meters. This power level is hard to directly drive a conventional wireless sensor in active mode. In the actual situation, the power density may be even lower due to the losses caused by cables and surrounding obstacles.

III. DESIGN AND IMPLEMENTATION OF THE BATTERY-LESS WIRELESS SENSOR TAG (BLWST)

This section is organized as follows. In Part A, we introduce the RF power source used in this study and analyze the characteristics of the propagation of the RF power. Part B discusses the diode selection. The characteristics of the DVM are analyzed in Part C. Part D and Part E present the design of the EWS and the power management strategy. The design of the impedance matching network is described in Part F.

A. Principle of the Dickson Voltage Multiplier (DVM)

The RF power harvested by the antenna is alternate, and its amplitude is attenuated rapidly as it travels, as shown in Fig. 3. At a far distance, the available voltage is usually insufficient to directly power the EWS. Thus, a voltage multiplier is necessary to generate a satisfied DC voltage. There are two types of frequently-used voltage multipliers, i.e., Cockcroft–Walton voltage multiplier and DVM [35]. We herein chose the latter one because the input capacitance is enlarged by the parallel arrangement of the capacitors, which allows smaller stage capacitors to be used [36]. Figure 4 shows the structure of the DVM, in which each stage consists of two diodes and two capacitors. The operation of the DVM is described as follows. L_m and C_m are components for impedance matching. An RF power source provides charging power. To understand the operation of the DVM, we assume that the components are ideal. During the initial half-cycle (negative), the diodes ($D_1, D_3 - D_{2N-1}$) are conducted. Therefore, the capacitors ($C_1, C_3 - C_{2N-1}$) will be charged to the voltage equal to the sum of the input voltage and the voltage of capacitors ($C_2, C_4 - C_{2N}$). Within the following half-cycle (positive), a total voltage of input voltage plus the voltage of the capacitors ($C_1, C_3 - C_{2N-1}$) will charge the capacitors ($C_2, C_4 - C_{2N}$) through diodes ($D_2, D_4 - D_{2N}$) [37]. As the polarity of the voltage source alternates, the voltage of the C_{2N} will be $2N$ times as much as the input voltage.

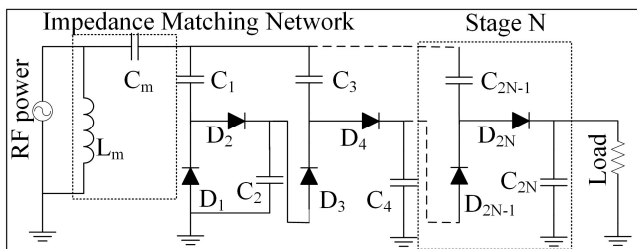


Fig. 4. The structure of the N -stage Dickson voltage multiplier. C_1 to C_{2N} are stage capacitors which store and deliver energy. D_1 to D_{2N} are diodes for rectification. The impedance matching network consisting of L_m and C_m matches the impedance of the voltage multiplier to that of the RF power source.

Ideally, more stages result in a higher output voltage. However, in the real situation, there is voltage loss caused by various factors, such as the voltage drop of the diode, the internal resistance of the component as well as the stray parameters. Consequently, more stages also cause more power loss. The practical output voltage can be estimated by (2) [38],

$$V_{out} = 2N \left(\frac{V_{in} C_c}{C_c + C_s} - V_d \right) - \frac{2NI_L}{(C_c + C_s)f} \quad (2)$$

where N is the number of the stage. V_{in} is the input voltage of the multiplier. C_c and C_s represent the stage capacitor and parasitic capacitance per stage. The voltage drop induced by each diode is V_d . I_L is the load current whereas f is the target frequency. The efficiency of the DVM is related to the number of the stage, the

load resistance, and the input power as well. The efficiency can be computed via (3),

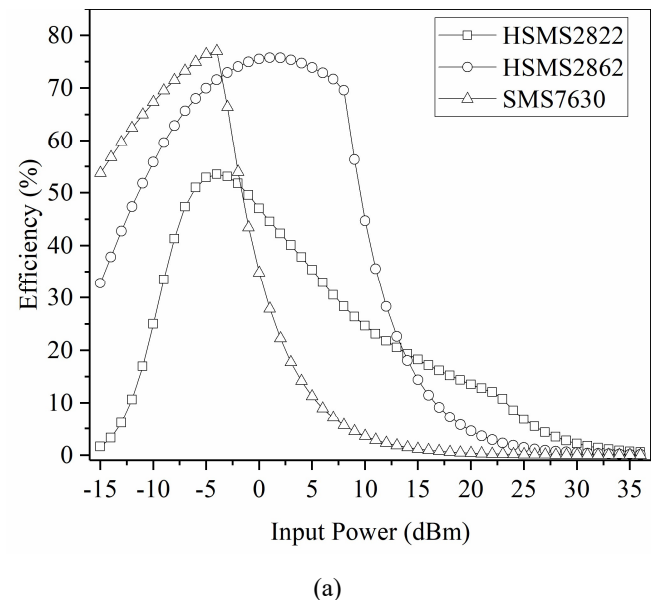
$$\eta_{pc} = \frac{V_{out}^2}{RP_{in}} \quad (3)$$

where R and P_{in} are the load resistance and input power, respectively.

According to (2) and (3), it is known that the diode voltage drop and the number of the stage affect the performance of the DVM. So we conducted simulation and experiment to select the appropriate diodes and the number of the stage, which will be presented in the following subsections.

B. Diode Selection for the Dickson Voltage Multiplier (DVM)

Diode is the key component of the voltage multiplier. Schottky diode is preferred because it has a very fast switching time and a low turn-on voltage compared to the normal diodes [39]. A low turn-on voltage contributes to a low voltage drop, which reduces the power loss of the voltage multiplier. Another consideration is the reverse breakdown voltage of the diode since the diode cannot work properly when the reverse voltage exceeds the rated value. We chose three different diodes, including SMS-7630, HSMS-2862, and HSMS-2822 with reverse breakdown voltages of 2 V, 7 V, and 15 V and turn-on voltages of 0.24 V, 0.35 V, and 0.34 V, respectively. We constructed the 1-stage DVM using the above three types of diodes and simulated the performance through Harmonic Balance Analysis in Advanced Design System. Each type of diodes was modeled according to the SPICE data provided by the manufacturers. Figure 5(a) shows the simulated efficiency based on different diodes. The efficiency is calculated by (3). Figure 5(b) is the structure of the 1-stage DVM for simulation. We finally chose HSMS-2862 since it has the best overall performance.



(a)

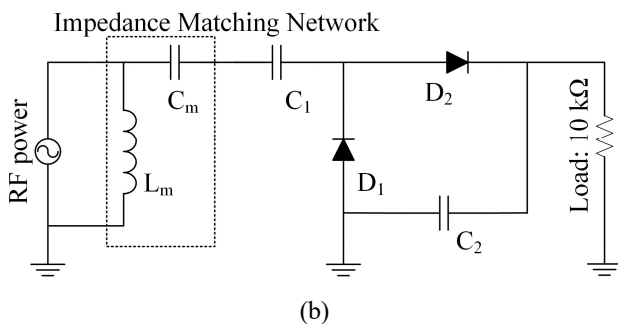


Fig. 5. Simulation of 1-stage Dickson voltage multiplier (DVM) constructed with different diodes. The load resistance is $10\text{ k}\Omega$ and the input power is swept from -15 to 36 dBm whereas the impedance of DVM is matched to $50\text{ }\Omega$ at the input power of -6 dBm. (a) Simulated efficiency. (b) Schematic of 1-stage DVM. C_1 and C_2 are stage capacitors; D_1 and D_2 are diodes for rectification; C_m and L_m are components for impedance matching.

C. Optimal Stage Number of Dickson Voltage Multiplier (DVM)

To decide the optimal stage, we soldered the diodes and capacitors on the fabricated printed circuit board (PCB) with a thickness of 1.6 mm and a dielectric ϵ_r of 4.5. The input current of the power management unit within the range of 800 nA to 900 nA for an input voltage from 3 V to 4 V in its sleep state, according to [40], will result in equivalent resistance of $3.75\text{ M}\Omega$ to $4.4\text{ M}\Omega$. Therefore, we used a resistor of $4.3\text{ M}\Omega$ as the load. The impedance of the circuit board was matched close to $50\text{ }\Omega$ through the impedance matching network. During the experiment, we connected the PCB to the signal generator (ADF4350) and recorded the voltage across the resistor with sweeping the input power from -15 dBm to 10 dBm.

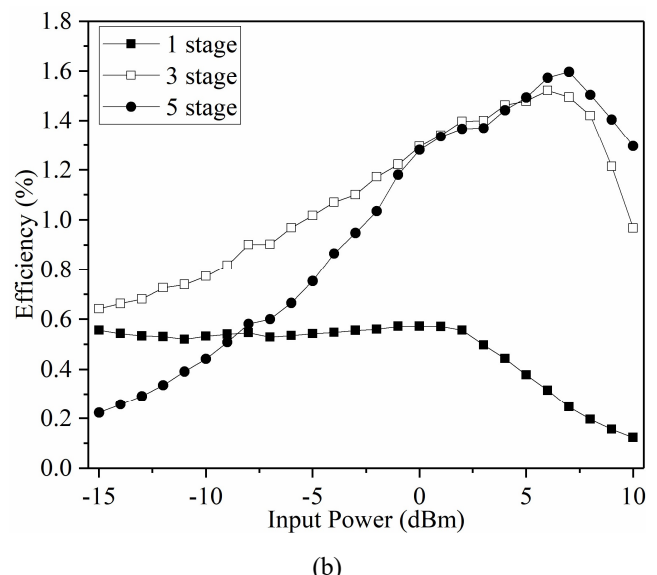
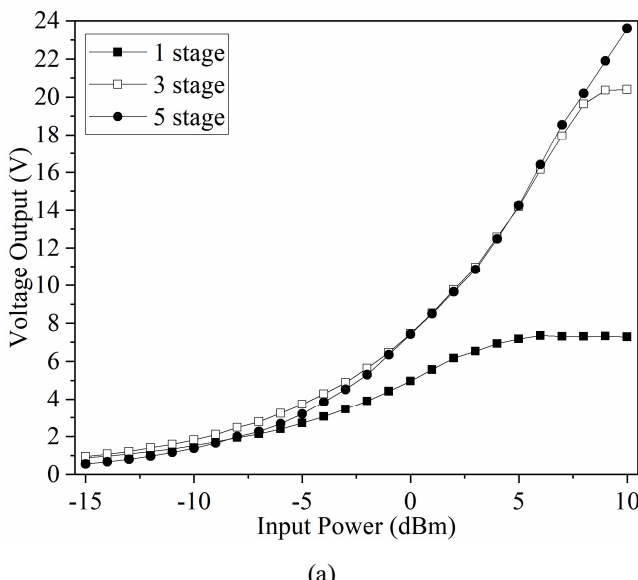


Fig. 6. Measured output voltages and efficiencies of 1-, 3- and 5-stage Dickson voltage multipliers. (a) Measured output voltage. (b) Measured efficiency. Each circuit is soldered on the fabricated PCB with impedance matched to $50\text{ }\Omega$ at the input power of -6 dBm. The frequency of the input power is 915 MHz, and the load is a resistor of $4.3\text{ M}\Omega$.

Figure 6 shows the measured output voltage and efficiency of the DVM with different stages. The efficiency is calculated via (3). As shown in Fig. 6(a), the 3-stage DVM produces the highest voltage in the low power region. The difference between the output voltages of the 3-stage and 5-stage DVMs can be negligible in the power range of 0 dBm to 5 dBm. When the input power exceeds 8 dBm, the output voltage of the 5-stage DVM maintains growth while that of the 3-stage DVM remains at 20 V. The 1-stage DVM has a lower output voltage compared to the others especially when the input power overtakes -5 dBm. We can observe from the curve of the 1-stage DVM that the output voltage keeps at approximately 7 V as the input power is greater than 5 dBm. As shown in Fig. 6(b), the efficiency of every DVM will rise at first but begin to fall at a certain input power. The efficiencies of the 3-stage and 5-stage DVMs show a significant drop when their input powers exceed 7 dBm. The efficiency of the 1-stage DVM decreases slightly until the input power reaches 2 dBm at which the efficiency begins to decline rapidly.

The stagnation of voltage increment and the drop in efficiency observed in Fig. 6 can be explained by the limitation of the diode. It is noted that the breakdown voltage of the diode used in the DVM is 7 V. The voltage no longer increases once the voltage across a single diode is higher than 7 V, resulting in the drop of efficiency. Overall, compared to the 3-stage DVM, there is no significant gain in voltage and efficiency of the 5-stage DVM. Therefore, we selected the 3-stage DVM for this design.

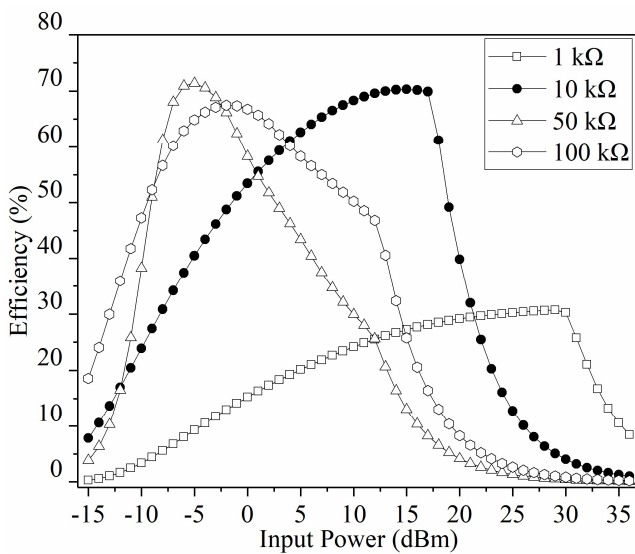


Fig. 7. Simulated efficiencies under different loads and input powers using Advanced Design System. The impedance is matched to $50\ \Omega$ for each load at the input power of -6 dBm . As the input power increases, the efficiency will rise at first with the slope decreasing until the efficiency peak emerges at a certain point.

Another factor determining the efficiency is the load. We used the Advanced Design System to simulate the impact of the load on the efficiency of the 3-stage DVM. The diode HSMS-2862 was modeled based on the spice model. As shown in Fig. 7, it can be observed that optimal loads exist in different power regions. In the lower power region, the load of $50\text{ k}\Omega$ produces the highest efficiency whereas the load of $10\text{ k}\Omega$ results the best performance in the higher power region. The peak efficiencies of $50\text{ k}\Omega$ and $100\text{ k}\Omega$ loads occur at around the input power of -5 dBm . As the load resistance decreases, the corresponding peak efficiency moves to a higher power region. The remarkable fall of the efficiency at the high power region is due to the limitation of the reverse breakdown voltage (7 V) of the diode. The diode will malfunction when the reverse voltage across the diode exceeds the rated one, which causes the decline of the efficiency.

D. Design of the Embedded Wireless Sensor (EWS)

In the case of a far distance, the available power is normally at the level of μW , which cannot support a general wireless sensor in the active mode. Therefore, to ensure a far operation range, the energy consumption of the wireless sensor should be as low as possible. The system-on-chip microcontroller CC430F5137 [41] integrated with an RF transceiver core, working at 433 MHz and consuming a minimum current of $2\ \mu\text{A}$ in the deep sleep mode with a 1.8 V supply voltage was determined. And the ADXL362 [42], an energy-efficient accelerometer with ultra-low power consumption ($1.8\ \mu\text{A}$ @ 2 V) was connected to the microcontroller through a serial peripheral interface (SPI). During operation, the microcontroller instructs the accelerometer to sense the acceleration of the tracks' vibration before the

accelerometer feeding back the measured data to the microcontroller. The data will be transmitted through the RF transceiver core.

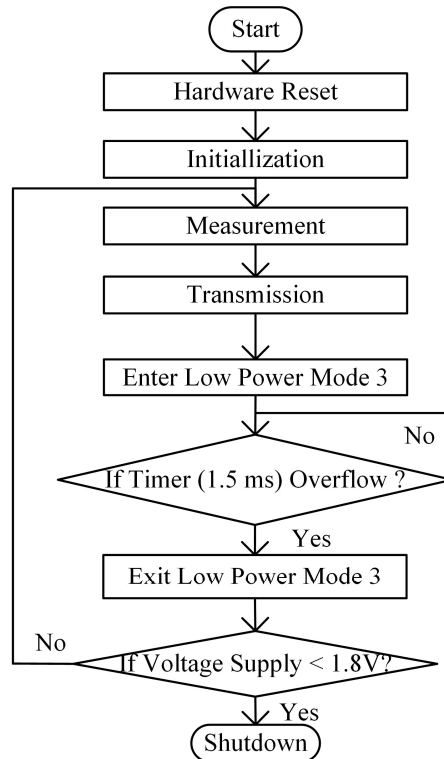


Fig. 8. Flow chart of the operation program. The source code of the operation program will be presented in the supplementary material.

A well-designed program is also necessary for reducing the power consumption. In the proposed application, the expected response time of the wireless sensor is very short. We chose the main clock frequency of 8 MHz , which is the maximum reachable frequency under the limitation of the 1.8 V supply voltage, to ensure a successful transmission of the data before running out of energy. Figure 8 is the flow chart of the program. Once the microcontroller is powered on, it executes the measurement and transmission instructions after finishing the initialization. Each transmission of the data packet includes six bytes of acceleration data, one byte of ID code, and one byte of verification code. Then, the microcontroller will enter the low power mode 3, in which the CPU will be turned off and only a timer will count for the next working cycle. The working cycle is defined as the interval between the adjacent transmissions of the data. If the power supply remains, the system will be periodically wakened up by the interrupt from the timer to implement the next working cycle.

E. Power Management of the Embedded Wireless Sensor (EWS)

Power management is crucial for a battery-free system. To measure the power consumption of the EWS, we first acquired

the current consumption by measuring the voltage across a $2.2\ \Omega$ resistor inserted into the power line of the EWS under a 1.8 V supply voltage. Figure 9 records the measured current consumption of the EWS. It can be observed that the time required for the start-up to the end of the first transmission is around 0.008 s , and the energy consumption (E_{EWS}) of $42.5\ \mu\text{J}$ during this period is calculated by (4),

$$E_{EWS} = \int_0^t V_{EWS} * I_{EWS} \quad (4)$$

where t (0.008 s) is the duration time from the start-up to the first transmission; V_{EWS} (1.8 V) and I_{EWS} are the supply voltage and current consumption of the EWS.

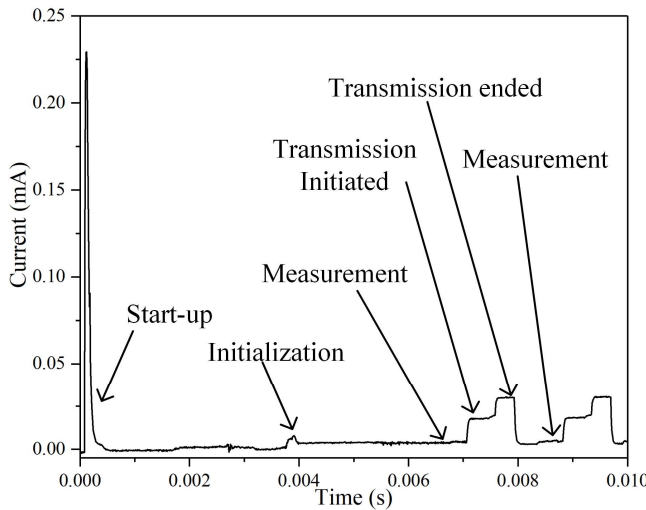


Fig. 9. Measured current consumption of the embedded wireless sensor (EWS). The power supply is 1.8 V . The activation of EWS draws the highest current, which is the inrush current caused by the charging of the EWS core. After initialization, the microcontroller enters the phase of measuring the acceleration and packaging the data. Another peak current occurs and remains until the end of the data transmission. The time required from start-up to the first transmission is around 0.008 s whereas the interval between adjacent transmissions is about 0.002 s .

Before the start-up of the EWS, there are some capacitors to be charged for supporting the running of the hardware, which leads to the large inrush current as shown in Fig 9. Consequently, the EWS may never be fully activated by the regulating circuit directly unless the input energy is sufficient. Therefore, the strategy for activating the EWS is to store the energy into a capacitor firstly until the energy level meets the requirement. A typical solution is to monitor the voltage across the storage capacitor by a voltage supervisor and stabilize the voltage by a voltage regulator. Once the voltage reaches the threshold, the voltage regulator will be enabled by the supervisor.

An off-the-shelf power management unit LTC3588-1 for efficient energy storage and conversion was selected. This power management unit features the functions of a wide hysteresis voltage supervisor and a buck converter, with an efficiency (η_{dc}) approximately 82% [40]. The output voltage of

the power management unit was set to 1.8 V and the storage capacitor was parallelly connected to the input ports of the power management unit. During operation, the power management unit remains a high impedance state to minimize the leakage current while the storage capacitor is being charged. Once the voltage of the storage capacitor exceeds an upper threshold ($V_{high} = 4\text{ V}$), the stored energy in the capacitor will be extracted by the power management unit to drive the EWS, which results in the dropping of the voltage across the storage capacitor. The power management unit stops consuming the energy and closes the output ports when the voltage of the storage capacitor declines to a lower threshold ($V_{low} = 3\text{ V}$), allowing energy to be collected in the storage capacitor again, as shown in Fig. 14.

The capacitance of the capacitor should be carefully chosen since larger capacitance requires longer charging time while smaller capacitance cannot activate the EWS. We calculated the energy consumption ($E_{EWS} = 42.5\ \mu\text{J}$) of EWS during the period from the start-up to the first transmission according to (4). Therefore, the minimum required capacitance can be estimated by (5).

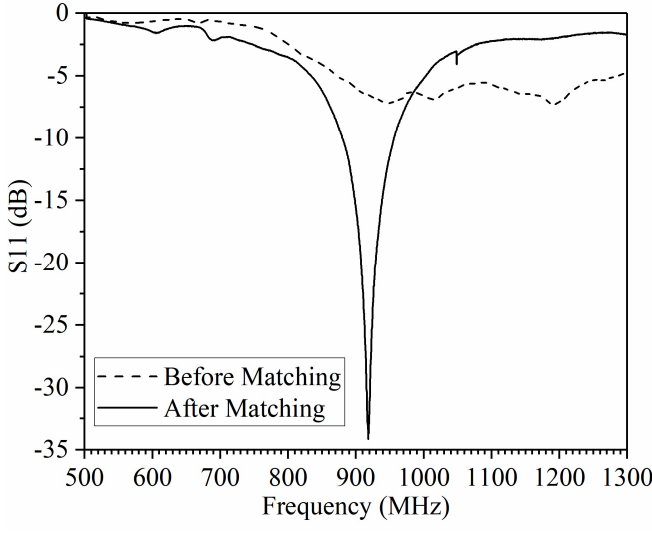
$$C_{storage} > 2E_{EWS} * (V_{high}^2 - V_{low}^2) / \eta_{lc} \quad (5)$$

Substituting the known parameters into (5), the $C_{storage}$ should be larger than $14\ \mu\text{F}$. We changed the capacitance of the storage capacitor around $14\ \mu\text{F}$ and found that a Nichicon UKL1H150KEDANA aluminum electrolytic capacitor [43] with a capacitance of $15\ \mu\text{F}$ exactly meets the requirements.

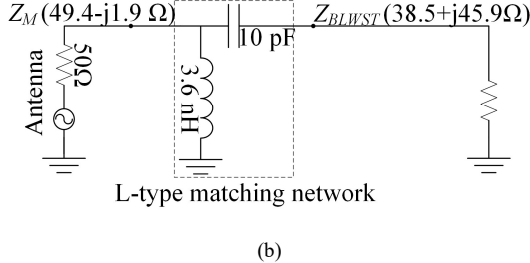
F. Design of Impedance Matching Network

The maximum power could be delivered from the source to the load when the input impedance of the load and the impedance of the antenna are complex conjugates at the working frequency [39]. The input impedance varies with the frequency and input power. We matched the input impedance of BLWST at 915 MHz and under the input power of -6 dBm since a high input power will offset the power losses caused by the impedance mismatch [36]. A vector network analyzer (mini VNA Tiny Plus2) calibrated before the measurement was used to measure the impedance. The unmatched input impedance (Z_{BLWST}) of BLWST was tuned close to $50\ \Omega$ to minimize the power loss. As shown in Fig. 10(b), the L-type matching network only consisting of two components was applied to match the impedance at the frequency of 915 MHz . Firstly, we measured that Z_{BLWST} equals $38.5 + j45.9\Omega$ using the vector network analyzer with the output power of -6 dBm . Then, we theoretically calculated the parameters of the two lumped-element components (2.6 pF for the series capacitor and 15.9 nH for the parallel inductor). However, the measured impedance of the PCB soldered with these two components deviates from the expected value due to the parasitic effect and non-linearity of the circuit. Finally, a series capacitor (10 pF) and a parallel inductor (3.6 nH) were experimentally found to

achieve the matched input impedance ($49.4 - j1.9\Omega$) of the BLWST (Z_M), as shown in Fig. 10(b). Figure 10(a) shows the return loss (S_{11}) of the BLWST measured by the vector network analyzer. After impedance matching, the return loss of 34 dB at 915 MHz was obtained, which indicates that 1.9% of the input power was reflected from the load under the input power of -6 dBm.



(a)

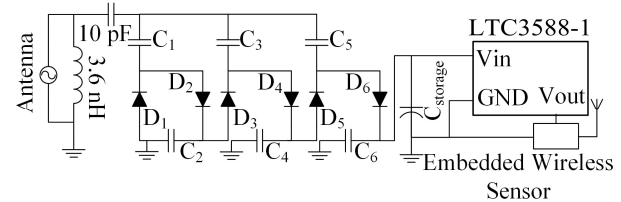


(b)

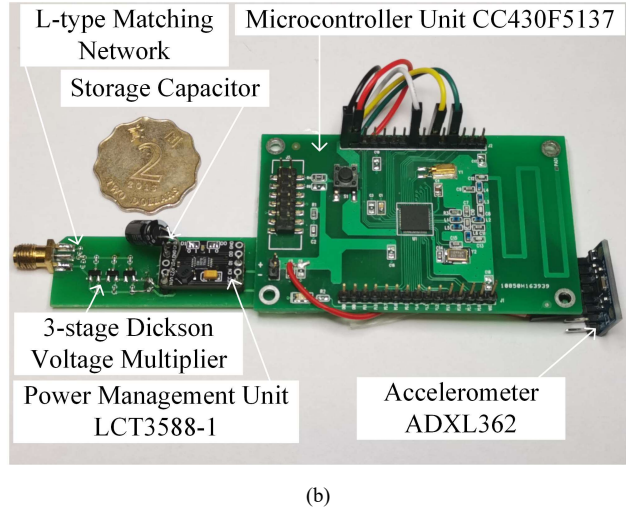
Fig. 10. Measured return loss and the L-type matching network. (a) Measured return loss under input power of -6 dBm. (b) L-type matching network. Z_{BLWST} is the unmatched input impedance of the battery-less wireless sensor tag whereas Z_M is the matched one. The matching network consists of a chip inductor (Murata, LQP15) and a chip capacitor (Murata, GJM155).

IV. PERFORMANCE EVALUATION

In this section, the performances of the 3-stage DVM and the BLWST at different distances were evaluated through experiments. Figure 11(a) presents the configuration of the BLWST with an antenna. $D_1 - D_6$ (HSMS-2862) are diodes for rectification and $C_1 - C_6$ (47 pF) are the stage capacitors. The output energy of the DVM will be stored in the storage capacitor $C_{storage}$ (15 μ F) and extracted by the LTC3588-1 to power the EWS when needed. Figure 11(b) shows the prototype of fabricated BLWST.



(a)



(b)

Fig. 11. The proposed battery-less wireless sensor tag. (a) Schematic, (b) Prototype.

A. Performance of the 3-Stage Dickson Voltage Multiplier (DVM) at Different Distances

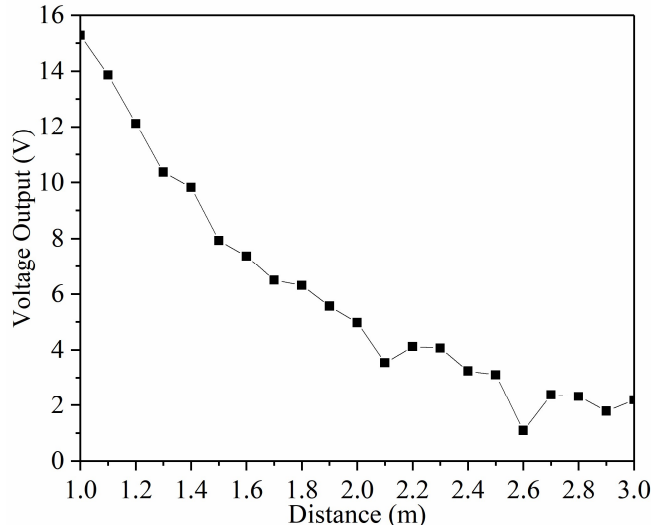
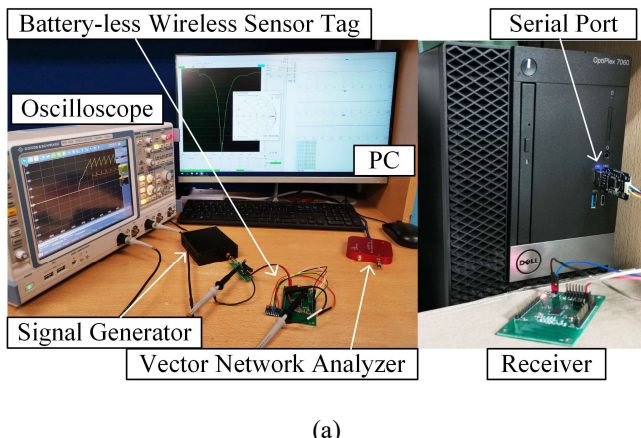


Fig. 12. Measured output voltage of the 3-stage Dickson voltage multiplier (DVM) as a function of the distance from the DVM to RF power source. The load is $4.3 \text{ M}\Omega$ and the distance increases from 1 meter with a step of 0.1 meters. The impedance of the DVM is matched to around 50Ω and connected to an omnidirectional antenna with a gain of 3 dBi.

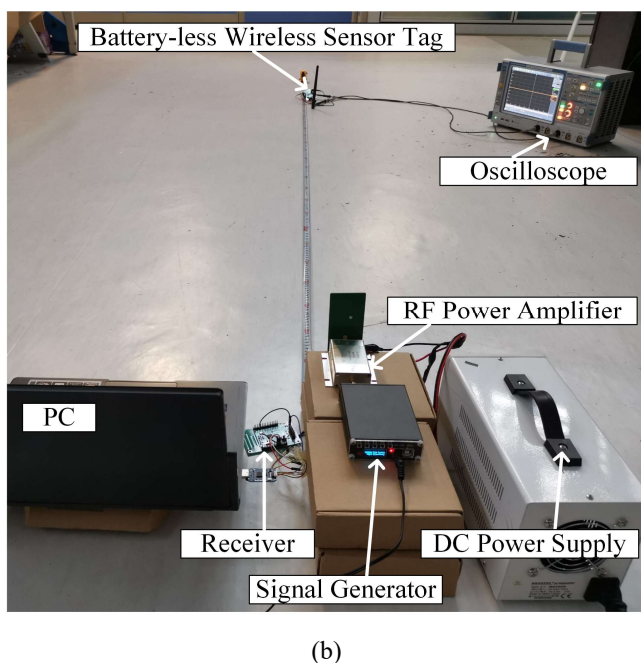
Figure 12 depicts the measured output voltage of the 3-stage DVM at different distances. The method of measurement is described in Fig. 13(b). We changed the distance and recorded

the measured output voltage across the load. In general, the output voltage and its slope decrease as the distance extends, although there are some notches in the voltage curve, such as the voltage at 2.6 m. This phenomenon can be explained by the multipath effect that the scattered RF power from the environment may cause a higher power density at a certain distance.

B. Performance of the Battery-Less Wireless Sensor Tag (BLWST)



(a)



(b)

Fig. 13. The experimental setup for performance evaluation. A receiver receives and uploads the data to the computer through the serial port. The accelerometer was arranged in a fixed posture so that we can validate the received data. (a) A signal generator (ADF4350) was used to generate sweeping power at 915 MHz. A Schwarz RTE 1024 oscilloscope was used to measure the voltages across the storage capacitor and the voltage supply of the EWS. (b) The customized RF power source consisting of the signal generator (ADF4350), the RF power amplifier (PF01411A), and a directional antenna with a gain of 6.1 dBi. The experimental space is $6 \times 2.5 \times 5$ m³ (length \times width \times height).

To investigate the performance of the BLWST, we conducted two experiments. As shown in Fig. 13(a), we swept the output power amplitude of the signal generator and recorded the waveform of the BLWST's output voltage. The purpose of this experiment is to observe the performance of the BLWST under different levels of input power. Another experiment shown in Fig. 13(b) is to evaluate the performance of the BLWST at different distances away from the RF power source. We observed that the minimum required input power for activating the BLWST is -4 dBm. Therefore, we swept the input power from -4 dBm to 10 dBm with a 1 dBm step and recorded the voltage. Figure 14 shows the waveforms recorded by the oscilloscope where V_{cap} and V_{dd} represent the voltage of the storage capacitor and the voltage supply of the BLWST, respectively. It can be seen that the pulse width of V_{dd} remains for approximately 0.008 s, which is exactly the time required for the EWS to successfully transmit the first data packet, as shown in Fig. 9.

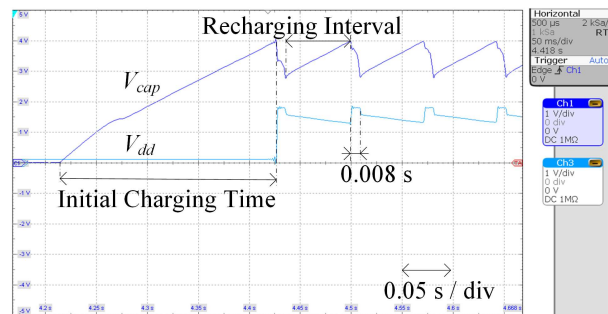
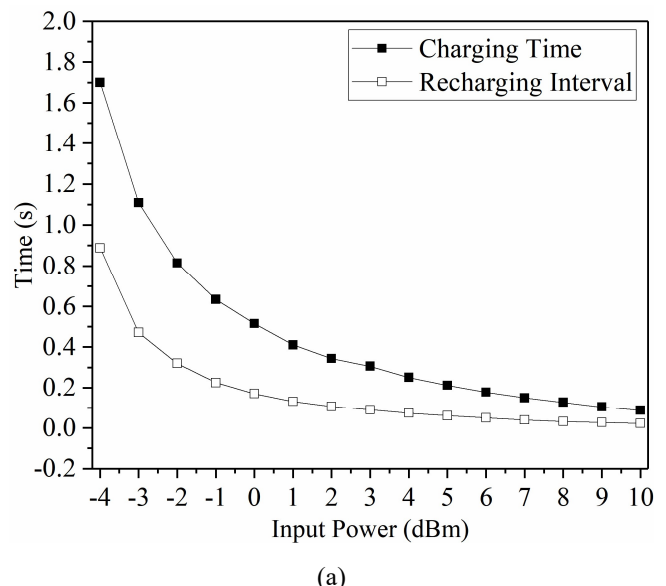


Fig. 14. The measured voltage of the storage capacitor (V_{cap}) and the voltage supply of the battery-less wireless sensor tag (V_{dd}) with an input power of 5 dBm. The initial charging time is the duration for the storage capacitor to be charged from 0 V to 4 V. The recharging interval is defined as the required time for the storage capacitor to be recharged from approximately 3 V to 4 V. Each of the pulse widths of V_{dd} remains for 0.008 s, indicating that the embedded wireless sensor is activated for 0.008 s during every working cycle.



(a)

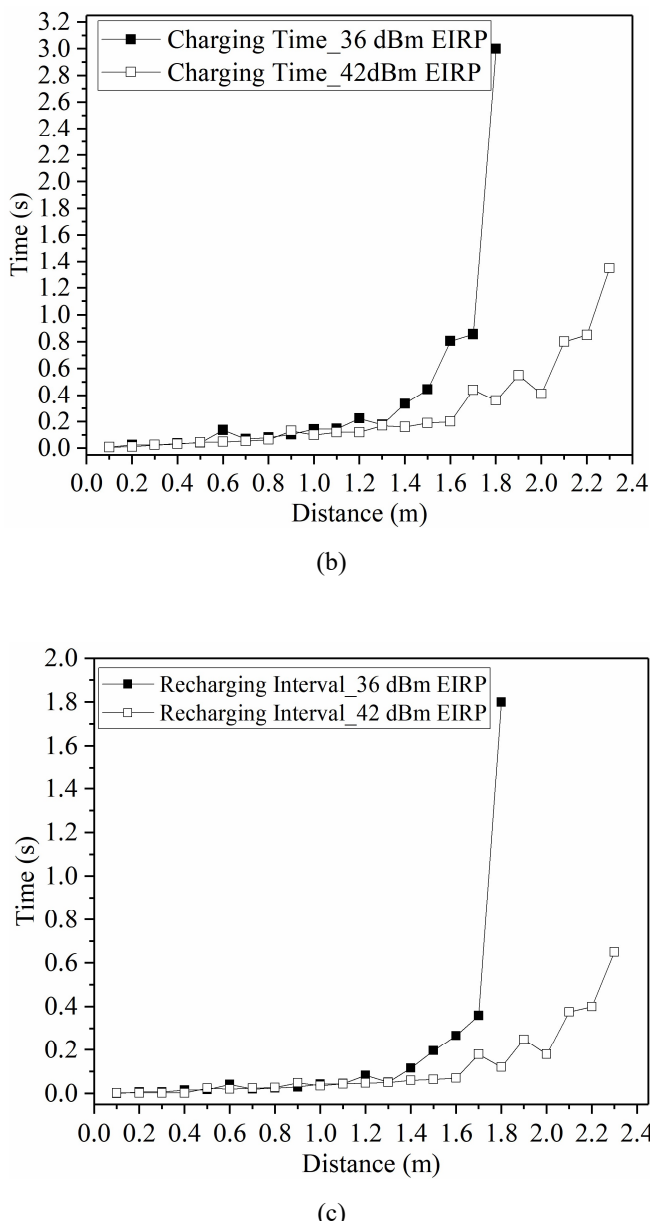


Fig. 15. Measured charging time and recharge interval. (a) Charging time and recharge interval varying with input power. As the input power steps up, the time required for charging and the recharging interval decreases. (b) Charging time changing with the distance between the RF power source and the battery-less wireless sensor tag. The power sources are 36 dBm EIRP and 42 dBm EIRP respectively. The distance initiates at 0.1 meters and increases with a step of 0.1 meters. Longer distance results in lower input power, and therefore longer charging time. (c) Recharging interval changing with the distance between the RF power source and the battery-less wireless sensor tag. The power sources are 36 dBm EIRP and 42 dBm EIRP. The trend of charging interval is similar to that of charging time.

As shown in Fig. 15(a), the minimum required input power for the start-up of the BLWST is -4 dBm. As expected, the higher the input power, the shorter the charging time and recharging interval. Under a 10 dBm input power, the charging time and recharging interval are 0.088 s and 0.027 s. Figures 15(b) and (c) describe the time required for charging and recharging the storage capacitor at different distances. The

maximum distance that allows the BLWST to be activated is 2.3 meters when the EIRP is 42 dBm. For 36 dBm EIRP, the farthest working distance is 1.8 meters. At a 0.2-meter distance, it only consumes 0.008 s for activating the BLWST. During the experiment, we observed that the input power is enough to supply the continuous operation of the proposed BLWST within a distance of 0.1 to 0.2 meters.

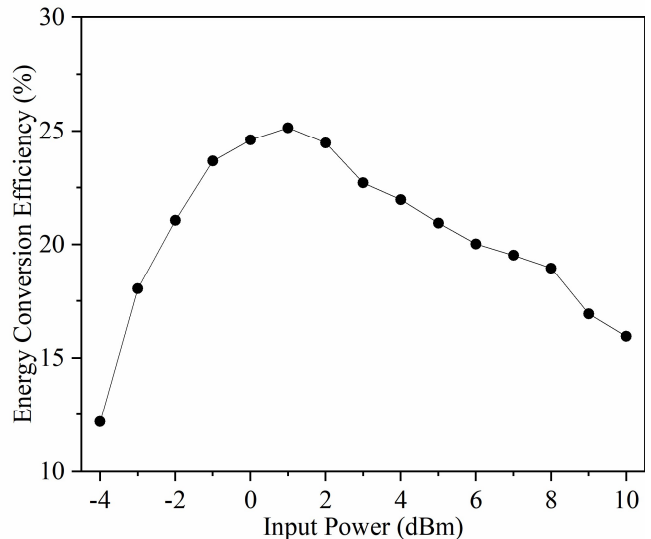


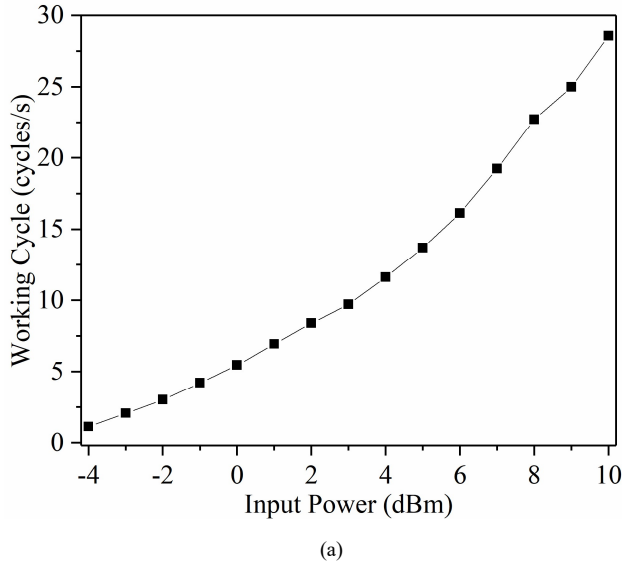
Fig. 16. Energy conversion efficiency of the battery-less wireless sensor tag during the period of recharging. The peak efficiency occurs at around 1 dBm.

The energy conversion efficiency of the BLWST can be estimated by the ratio of the energy delivered to the load (EWS) to the sum of the input energy from the signal generator, as expressed in (6),

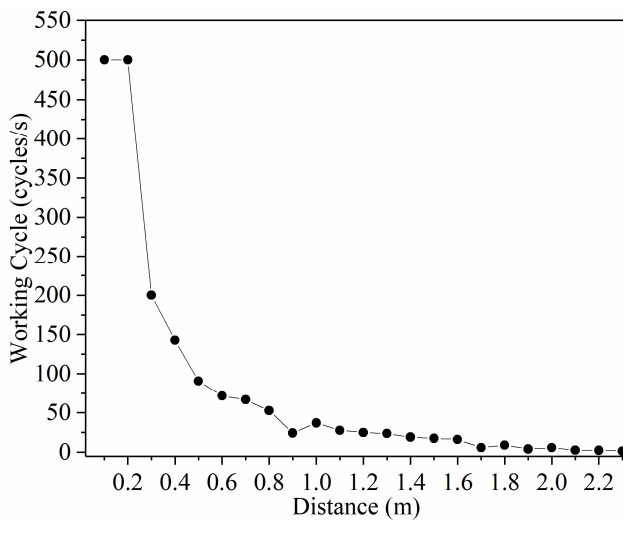
$$\eta_{BLWST} = \frac{\eta_{dc} C_{storage} (V_{high}^2 - V_{low}^2)}{2P_{in} t_c} \quad (6)$$

where η_{BLWST} is the energy conversion efficiency of the BLWST; t_c is the charging duration of storage capacitor from V_{low} to V_{high} through the 3-stage DVM under an RF input power of P_{in} , and thus the energy accumulated in the storage capacitor as well as the total input energy (P_{intc}) can be obtained. Subsequently, the LTC3588-1 extracts energy from the storage capacitor and delivers it to the EWS based on an efficiency of η_{dc} , with the voltage of the storage capacitor declining from V_{high} to V_{low} . The calculated η_{BLWST} is shown in Fig. 16. The overall efficiency is higher than 10% and the highest efficiency is approximately 25% under an input power of 1 dBm. Higher efficiency is possible to be achieved by some mechanisms. Each part of the BLWST including impedance matching network, voltage multiplier, power management circuit, and load will contribute to the overall efficiency. The lumped components used in the impedance matching circuit will induce power loss, so lumped components with higher quality factor (Q) and lower equivalent series resistance (ESR) can be applied to reduce the power loss. PCB made of lower dielectric loss materials will also increase

the overall efficiency. And diodes with lower turn-on voltage reduce the power loss brought by the voltage drop and therefore increase efficiency. Moreover, the efficiency of the current power management circuit is 82 %, which can be optimized further to promote overall efficiency.



(a)



(b)

Fig. 17. Working cycles per second. (a) Working cycles per second as a function of input power. (b) Working cycles per second at different distances under the EIRP of 42 dBm Within the range of 0.1 to 0.2 meters, we observed that the received power allows the embedded wireless sensor to work without interruption. Therefore, the interval should be about 2 ms as shown in Fig. 9, which results in 500 working cycles per second.

A shorter recharging interval results in more working cycles and more data can be gathered per unit time. The number of working cycles per second can be calculated via (7),

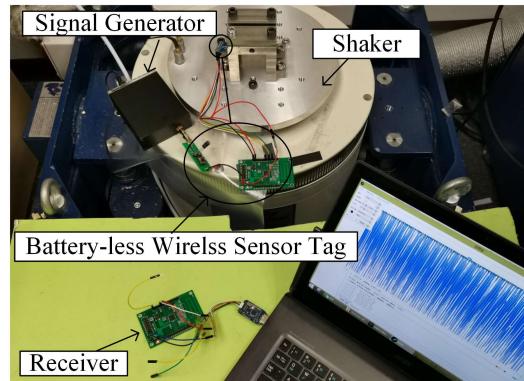
$$D = \frac{1}{T_{recharging} + 0.008} \quad (7)$$

where $T_{recharging}$ is the recharging interval. The interval between adjacent working cycles equals the sum of $T_{recharging}$ and 0.008 s, as shown in Fig. 14.

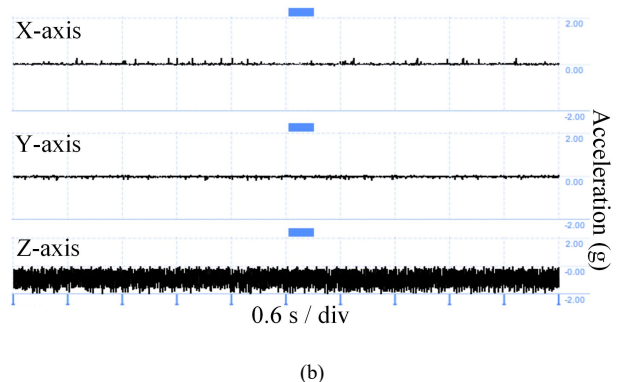
Figure 17 exhibits the working cycles per second calculated by (7). Up to 28 working cycles can be reached in one second under an input power of 10 dBm and 500 working cycles per second was recorded at the distance of 0.1 to 0.2 meters under the EIRP of 42 dBm.

C. Vibration Monitoring

The proposed design overcomes the challenge of the battery-less monitoring of the railway tracks by utilizing the RF power to remotely drive the BLWST. We conducted a test to verify the performance of the remote acceleration measurement. We used a high precision L215M vibration shaker system from ETS Solutions to simulate the track's vibration with precise acceleration and frequency. Figure 18 shows the method and results of the test. Powered by the signal generator, the BLWST measured the acceleration of the shaker and transmitted the data. The sent data will be captured by the receiver and uploaded to the laptop through a serial port. Due to the installation posture of the accelerometer, an initial acceleration of -1 g ($g = 9.8 \text{ m/s}^2$) along Z-axis was induced by gravity. As the acceleration of the shaker is set to 1 g, the acceleration along Z-axis was expected to fluctuate within the range of -2 g to 0 g. Figure 18(b) shows that the obtained accelerations along Z-axis are all within -2 g to 0 g, as expected.



(a)



(b)

Fig. 18. Vibration measurement. (a) Experimental setup. The battery-less wireless sensor tag (BLWST) is driven by a signal generator (0 dBm @ 915 MHz). The measurement range of the accelerometer is programmed to ± 2 g. The acceleration and frequency of the vibration generated by the shaker are 1 g ($g = 9.8 \text{ m/s}^2$) and 20 Hz respectively. The accelerometer was fixed on the fixture with its Z-axis direction downward. (b) Real-time measured acceleration data received from the BLWST. The real-time plotting is achieved by an open-source software (VODKA).

V. APPLICATION

Figure 19 shows a demo of the proposed railway tracks monitoring system (see Supplementary Video 1).

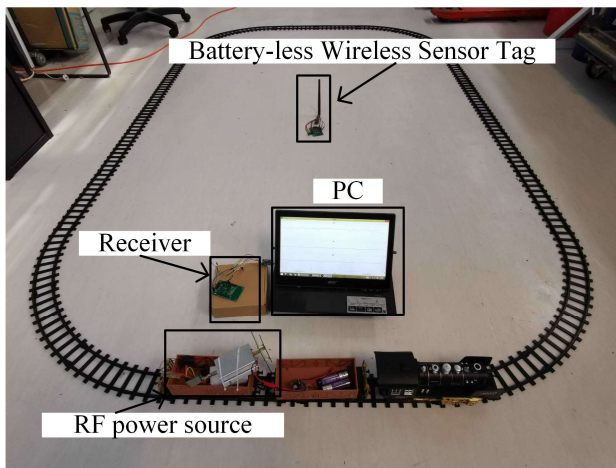


Fig. 19. Demo of the proposed railway tracks monitoring system based on RF energy harvesting, which consists of the battery-less wireless sensor tag installed on the tracks and the reader equipped on the train. In the demo, the received data is plotted on the PC in real-time. (see Supplementary Video 1).

In the actual application scenario, the speed of the train is considerable fast. For example, the highest running speed of the Airport Express in Hong Kong can be 135 km/h [44]. The current test result shows that the BLWST can be activated within 0.008 ms and transmit the measured acceleration data within another 0.008 s. Then, the system worked continuously, keeping an interval of 0.002 s between adjacent transmissions. Assuming a train with 100 meters in length, it will spend around 2.6 s to travel for 100 meters with a speed of 135 km/h. By periodically arranging the RF power sources on the train, it is possible to ensure that the BLWST is always under the coverage of the sufficient RF power during the train passing by these BLWSTs. Consequently, approximately 1300 data packets can be acquired by a high-speed train. The discussion above only considers the ideal situation under normal speed. More dynamic experiments will be conducted to prove the performance of the proposed system at a very high speed in future work. And the experimental method can refer to [45] where a speed detection system using self-power Bluetooth SoC was evaluated on a conveyor belt.

VI. CONCLUSION

This paper presents an RF energy harvesting based on sensor system for structural health monitoring of rail tracks. The

advantages of the proposed system are of low cost and high inspection frequency. To our best knowledge, this is the first report on autonomous, wireless, battery-less, and maintenance-free system for railway inspection. The energy conversion efficiency of the designed BLWST can reach 25 %. The maximum working distance can be 2.3 meters and the minimum input power required to activate the BLWST is -4 dBm. Besides, up to 500 working cycles per second can be realized at a distance shorter than 0.2 meters. We have demonstrated the proposed system for vibration monitoring and rail track inspection. The RF energy harvesting capability can be further optimized by designing a high gain antenna. The efficiency of the BLWST can be promoted by improving the impedance matching network and utilizing diodes with lower turn-on voltage.

ACKNOWLEDGEMENTS

The work described in this paper is supported by the Early Career Scheme (No. CityU 21210619) from the Research Grants Council of the Hong Kong Special Administrative Region, National Natural Science Foundation of China (No. 11902282), and City University of Hong Kong (No. 9610390).

REFERENCES

- [1] J. J. Wang, G. Penamalli, and L. Zuo, "Electromagnetic energy harvesting from train induced railway track vibrations," in *Proceedings of 2012 IEEE/ASME 8th IEEE/ASME international conference on mechatronic and embedded systems and applications*, 2012: IEEE, pp. 29-34.
- [2] J. Lu, M. Gao, Y. Wang, and P. Wang, "Health monitoring of urban rail corrugation by wireless rechargeable sensor nodes," *Structural Health Monitoring*, vol. 18, no. 3, pp. 838-852, 2018, doi: 10.1177/1475921718782395.
- [3] L. Ferreira and M. H. Murray, "Modelling rail track deterioration and maintenance: current practices and future needs," *Transport Reviews*, vol. 17, no. 3, pp. 207-221, 1997.
- [4] V. J. Hodge, S. O'Keefe, M. Weeks, and A. Moulds, "Wireless sensor networks for condition monitoring in the railway industry: A survey," *IEEE Transactions on Intelligent Transportation Systems*, vol. 16, no. 3, pp. 1088-1106, 2014.
- [5] Q. Li, Z. Zhong, Z. Liang, and Y. Liang, "Rail inspection meets big data: methods and trends," in *2015 18th International Conference on Network-Based Information Systems*, 2015: IEEE, pp. 302-308.
- [6] S. Moustakidis, V. Kappatos, P. Karlsson, C. Selcuk, T.-H. Gan, and K. Hrissagis, "An Intelligent Methodology for Railways Monitoring Using Ultrasonic Guided Waves," *Journal of Nondestructive Evaluation*, vol. 33, no. 4, pp. 694-710, 2014, doi: 10.1007/s10921-014-0264-6.
- [7] R. Clark, "Rail flaw detection: overview and needs for future developments," *NDT & E International*, vol. 37, no. 2, pp. 111-118, 2004, doi: 10.1016/j.ndteint.2003.06.002.
- [8] Z. Liu, W. Li, F. Xue, J. Xiafang, B. Bu, and Z. Yi, "Electromagnetic Tomography Rail Defect Inspection," *IEEE Transactions on Magnetics*, vol. 51, no. 10, pp. 1-7, 2015, doi: 10.1109/tmag.2015.2430283.
- [9] M. Hughes, "Trimming the cost of track inspection," *Railway Gazette International*, vol. 166, no. 11, pp. 43-46, 2010.
- [10] A. E. Loulou *et al.*, "Multiplierless filtered-OFDM transmitter for narrowband IoT devices," *IEEE Internet of Things Journal*, 2019.
- [11] C. Ngamkhanong, S. Kaewunruen, and B. Costa, "State-of-the-Art Review of Railway Track Resilience Monitoring," *Infrastructures*, vol. 3, no. 1, 2018, doi: 10.3390/infrastructures3010003.
- [12] C.-B. Yun and J. Min, "Smart sensing, monitoring, and damage detection for civil infrastructures," *KSCE Journal of Civil Engineering*, vol. 15, no. 1, pp. 1-14, 2010, doi: 10.1007/s12205-011-0001-y.

- [13] M. Gao, P. Wang, Y. Wang, and L. Yao, "Self-Powered ZigBee Wireless Sensor Nodes for Railway Condition Monitoring," *IEEE Transactions on Intelligent Transportation Systems*, vol. 19, no. 3, pp. 900-909, 2018, doi: 10.1109/tits.2017.2709346.
- [14] F. K. Shaikh and S. Zeadally, "Energy harvesting in wireless sensor networks: A comprehensive review," *Renewable and Sustainable Energy Reviews*, vol. 55, pp. 1041-1054, 2016.
- [15] M. Kiziroglou, D. Boyle, S. Wright, and E. Yeatman, "Acoustic power delivery to pipeline monitoring wireless sensors," *Ultrasonics*, vol. 77, pp. 54-60, 2017.
- [16] V. Misra *et al.*, "Optimizing the energy balance to achieve autonomous self-powering for vigilant health and IoT applications," in *Journal of Physics: Conference Series*, 2019, vol. 1407, no. 1: IOP Publishing, p. 012001.
- [17] B. Kathpalia, D. Tan, I. Stern, and A. Erturk, "Evaluation of human-scale motion energy harvesting for wearable electronics," in *Active and Passive Smart Structures and Integrated Systems 2017*, 2017, vol. 10164: International Society for Optics and Photonics, p. 101641H.
- [18] R. Shigeta *et al.*, "Ambient RF energy harvesting sensor device with capacitor-leakage-aware duty cycle control," *IEEE Sensors Journal*, vol. 13, no. 8, pp. 2973-2983, 2013.
- [19] S. Sudevalayam and P. Kulkarni, "Energy Harvesting Sensor Nodes: Survey and Implications," *IEEE Communications Surveys & Tutorials*, vol. 13, no. 3, pp. 443-461, 2011, doi: 10.1109/surv.2011.060710.00094.
- [20] R. Bischoff, J. Meyer, O. Enochsson, G. Feltrin, and L. Elfgen, "Event-based strain monitoring on a railway bridge with a wireless sensor network," in *Proceedings of the 4th International Conference on Structural Health Monitoring of Intelligent Infrastructure, Zurich, Switzerland*, 2009, vol. 2224, p. 7482.
- [21] Y. Tianchen, Y. Jian, S. Ruigang, and L. Xiaowei, "Vibration energy harvesting system for railroad safety based on running vehicles," *Smart materials and structures*, vol. 23, no. 12, p. 125046, 2014.
- [22] Y. Pan, F. Liu, R. Jiang, Z. Tu, and L. Zuo, "Modeling and onboard test of an electromagnetic energy harvester for railway cars," *Applied Energy*, vol. 250, pp. 568-581, 2019.
- [23] Z. Yang, S. Zhou, J. Zu, and D. Inman, "High-performance piezoelectric energy harvesters and their applications," *Joule*, vol. 2, no. 4, pp. 642-697, 2018.
- [24] A. K. Moghaddam, J. H. Chuah, H. Ramiah, J. Ahmadian, P.-I. Mak, and R. P. Martins, "A 73.9%-Efficiency CMOS Rectifier Using a Lower DC Feeding (LDCF) Self-Body-Biasing Technique for Far-Field RF Energy-Harvesting Systems," *IEEE Transactions on Circuits and Systems I: Regular Papers*, vol. 64, no. 4, pp. 992-1002, 2017, doi: 10.1109/tcsi.2016.2623821.
- [25] P. Broutas, H. Contopanagos, E. D. Kyriakis-Bitzaros, D. Tsoukalas, and S. Chatzandroulis, "A low power RF harvester for a smart passive sensor tag with integrated antenna," *Sensors and Actuators A: Physical*, vol. 176, pp. 34-45, 2012, doi: 10.1016/j.sna.2011.12.053.
- [26] C. M. Roberts, "Radio frequency identification (RFID)," *Computers & security*, vol. 25, no. 1, pp. 18-26, 2006.
- [27] L. Cui, Z. Zhang, N. Gao, Z. Meng, and Z. Li, "Radio Frequency Identification and Sensing Techniques and Their Applications-A Review of the State-of-the-Art," *Sensors (Basel)*, vol. 19, no. 18, Sep 17 2019, doi: 10.3390/s19184012.
- [28] B. Malakar and B. Roy, "Survey of RFID applications in railway industry," in *2014 First International Conference on Automation, Control, Energy and Systems (ACES)*, 2014: IEEE, pp. 1-6.
- [29] A. P. Sample, D. J. Yeager, P. S. Powledge, and J. R. Smith, "Design of a passively-powered, programmable sensing platform for UHF RFID systems," in *2007 IEEE International Conference on RFID*, 2007: IEEE, pp. 149-156.
- [30] J. Qian *et al.*, "A passive UHF tag for RFID-based train axle temperature measurement system," in *2011 IEEE Custom Integrated Circuits Conference (CICC)*, 2011: IEEE, pp. 1-4.
- [31] K. K. H. Lee and D. K. W. Chau, "Condition based monitoring in railway," *Journal of International Council on Electrical Engineering*, vol. 2, no. 1, pp. 99-103, 2012.
- [32] J. Mundrey, *Railway track engineering*. Tata McGraw-Hill Education, 2009.
- [33] D. De Donno, L. Catarinucci, and L. Tarricone, "An UHF RFID energy-harvesting system enhanced by a DC-DC charge pump in silicon-on-insulator technology," *IEEE Microwave and Wireless Components Letters*, vol. 23, no. 6, pp. 315-317, 2013.
- [34] R. He *et al.*, "High-speed railway communications: From GSM-R to LTE-R," *Ieee vehicular technology magazIne*, vol. 11, no. 3, pp. 49-58, 2016.
- [35] M. Cansiz, D. Altinel, and G. Karabulut Kurt, *Efficiency in RF energy harvesting systems: A comprehensive review*. 2019.
- [36] B. R. Marshall, M. M. Morys, and G. D. Durgin, "Parametric analysis and design guidelines of RF-to-DC Dickson charge pumps for RFID energy harvesting," in *2015 IEEE International Conference on RFID (RFID)*, 2015: IEEE, pp. 32-39.
- [37] S. Kim *et al.*, "Ambient RF Energy-Harvesting Technologies for Self-Sustainable Standalone Wireless Sensor Platforms," *Proceedings of the IEEE*, vol. 102, no. 11, pp. 1649-1666, 2014, doi: 10.1109/jproc.2014.2357031.
- [38] R. E. Barnett, J. Liu, and S. Lazar, "A RF to DC voltage conversion model for multi-stage rectifiers in UHF RFID transponders," *IEEE Journal of solid-state circuits*, vol. 44, no. 2, pp. 354-370, 2009.
- [39] Y. Shinki, K. Shibata, M. Mansour, and H. Kanaya, "Impedance Matching Antenna-Integrated High-Efficiency Energy Harvesting Circuit," *Sensors (Basel)*, vol. 17, no. 8, Aug 1 2017, doi: 10.3390/s17081763.
- [40] Linear Technology, LTC3588-1. [Online]. Available: <https://www.analog.com/cn/products/ltc3588-1.html>
- [41] Texas Instruments, CC430F5137. [Online]. Available: <http://www.ti.com/product/CC430F5137>
- [42] Analog Devices, ADXL362. [Online]. Available: <https://www.analog.com/cn/products/adxl362.html>
- [43] Nichicon, Aluminum Electrolytic Capacitor UKL. [Online]. Available: <https://www.mouser.cn/datasheet/2/293/e-ukl-1513439.pdf>
- [44] HKSAR Government. "Hongkong: The Facts - Railway Network." <https://www.gov.hk/en/about/abouthk/factsheets/docs/railway.pdf>
- [45] R. La Rosa, C. Dehollain, and P. Livreri, "Advanced Monitoring Systems Based on Battery-Less Asset Tracking Modules Energized through RF Wireless Power Transfer," *Sensors*, vol. 20, no. 11, p. 3020, 2020.